

Granular flow simulation in a centrifugal acceleration field

*Original*

Granular flow simulation in a centrifugal acceleration field / Cabrera, Miguel Angel; Leonardi, Alessandro; Peng, Chong. - In: GEOTECHNIQUE. - ISSN 0016-8505. - 70:10(2020), pp. 894-905. [10.1680/jgeot.18.p.260]

*Availability:*

This version is available at: 11583/2759946 since: 2020-11-17T18:42:44Z

*Publisher:*

ICE publishing

*Published*

DOI:10.1680/jgeot.18.p.260

*Terms of use:*

This article is made available under terms and conditions as specified in the corresponding bibliographic description in the repository

*Publisher copyright*

SPIIE [DA NON USARE]

Da definire

(Article begins on next page)

# Accepted manuscript doi: 10.1680/jgeot.18.p.260

---

## **Accepted manuscript**

As a service to our authors and readers, we are putting peer-reviewed accepted manuscripts (AM) online, in the Ahead of Print section of each journal web page, shortly after acceptance.

## **Disclaimer**

The AM is yet to be copyedited and formatted in journal house style but can still be read and referenced by quoting its unique reference number, the digital object identifier (DOI). Once the AM has been typeset, an 'uncorrected proof' PDF will replace the 'accepted manuscript' PDF. These formatted articles may still be corrected by the authors. During the Production process, errors may be discovered which could affect the content, and all legal disclaimers that apply to the journal relate to these versions also.

## **Version of record**

The final edited article will be published in PDF and HTML and will contain all author corrections and is considered the version of record. Authors wishing to reference an article published Ahead of Print should quote its DOI. When an issue becomes available, queuing Ahead of Print articles will move to that issue's Table of Contents. When the article is published in a journal issue, the full reference should be cited in addition to the DOI.

# Accepted manuscript doi: 10.1680/jgeot.18.p.260

---

**Submitted:** 09 October 2018

**Published online in ‘accepted manuscript’ format:** 14 August 2019

**Manuscript title:** Granular flow simulation in a centrifugal acceleration field

**Authors:** Miguel Angel Cabrera\*, Alessandro Leonardi<sup>†</sup> and Chong Peng<sup>‡</sup>

**Affiliations:** \*Universidad de los Andes, Department of Civil and Environmental Engineering, Carrera, Bogota, Colombia; <sup>†</sup>Politecnico di Torino, Department of Structural, Geotechnical and Building Engineering, Corso Duca degli Abruzzi, Torino, Italy and <sup>‡</sup>Engineering Software Steyr GmbH, Berggasse, Steyr, Austria

**Corresponding author:** Miguel Angel Cabrera, Universidad de los Andes, Department of Civil and Environmental Engineering, Carrera 1Este No. 19A-40, Bogota, Colombia.

**E-mail:** ma.cabrera140@uniandes.edu.co

**Abstract**

The use of the geotechnical centrifuge to obtain scaled physical models is a useful tool in geomechanics. When dealing with granular flows, however, the traditional scaling principles are challenged by the complex rheology of the material, and by the non-trivial effects of the Coriolis apparent acceleration. In a laboratory centrifuge, obtaining a clear understanding of these effects is further complicated by the technical difficulties in obtaining flows in steady conditions. In this work, we study the scaling principles for granular flows using a numerical model based on the Discrete Element Method. We are in this way able to obtain a steady flow in a rotating reference frame, and to explore the variation of macroscopic properties by changing the scaling factor and the distance from the rotation center. The outcome is compared with the prediction obtained with a continuum theory for frictional flows. Results show that granular flows scale consistently only when the Coriolis acceleration is negligible, and are severely altered otherwise. The augmented acceleration field is also responsible for an alteration of the flow state, driving the system towards the inertia-driven collisional regime.

**Keywords:** centrifuge modelling; constitutive relations; discrete-element modelling; slopes

## Introduction

Mass flows occurring in nature, like landslides, debris flows, rock avalanches, and mudflows, pose a constant threat to mountain communities worldwide (Hung & Jakob, 2005; Nadim *et al.*, 2006). They are a key challenge for many countries where social and economic development increases exposure, and where land-use faces dramatic changes (Marin-Ferrer *et al.*, 2017; Froude & Petley, 2018). These flows are composed of a mixture of sediment and water, in which the particle size distribution (PSD) and solid fraction govern the resultant flow dynamics.

These phenomena are particularly difficult to reproduce at the laboratory scale, due to their multiphase nature, which in turn determines the simultaneous presence of multiple physical effects. Most physical modelling is conducted on scaled artificial channels of a few meters. This implies that the material self-weight is much lower than in nature and that the shear-strain resistance between the solid and fluid phases is not proportionally scaled, a fact often overlooked when interpreting the results (Iverson, 2015). In nature, the flow weight controls multiple key aspects of the mechanism, such as the packing density and velocity of the mass flow. It also determines the intensity and duration of the particle and fluid interactions within the moving mass and against its confining boundaries, as well as the occurrence of phase separation, inverse segregation, erosion, and mass consolidation through all flow stages (e.g., initiation, translation, and deposition).

For all these reasons, the use of the geotechnical centrifuge to obtain a realistic stress field on the sample would be highly beneficial. Figure 1 presents an example of a centrifuge model for the study of granular flows. The sample is built by injecting grains from a container onto a flume. In this type of model, the flume is not tilted in the traditional sense, i.e. with respect to gravity, but rather with respect to the direction of the centrifugal acceleration, increasing the normal stress on the basal sliding plane. A common practice for interpreting this type of setup is to relate a scaling factor  $N$  to an equivalent field-scale event (e.g. prototype). Within this interpretation, geometric, kinematic, and dynamic similarities, known as scaling principles, are formulated between the scale-model and the prototype (Garnier *et al.*, 2007).

In spite of a well-established set of scaling principles for static and dynamic systems, the scaling principles formulated for kinematic processes are still under validation. Exploratory studies in this direction have been conducted in the past by Vallejo *et al.* (2006), Brucks *et al.* (2007), Gue (2012), Bowman *et al.* (2012), Ng *et al.* (2017), and Cabrera & Wu (2017a). All have faced challenges from a technological point of view (i.e., material mixing, triggering mechanism, feeding system, channel instrumentation), and theoretical complications arising from estimating the extent to which the curvature of the centrifugal acceleration field, and the non-inertial reference frame, affect the resultant mass flows and their relation with prototype events (Bryant *et al.*, 2015; Cabrera & Wu, 2016). These complications have become a fundamental priority with the rise of studies focusing on the impact forces of mass flows against obstacles, such as those conducted by Ng *et al.* (2017) and Song *et al.* (2017), where the up-scaling process of the experimental observations is not fully clear.

The complex interdependence of flow features, apparent forces, and unsteady effects have therefore greatly hampered efforts in this direction. To overcome this, we present results obtained with a numerical model based on the Discrete Element Method (DEM). We focus on steady and dense dry flows, leaving the complexity of the coupling with a fluid phase (Leonardi *et al.*, 2015, 2018) or the study of dilute flows (Bryant *et al.*, 2015) to a later study. This model greatly simplifies reality by enabling the generation of steady conditions and, most importantly, by allowing for the prescription of the imposed acceleration field on an ad-

hoc basis. In this way, the effects created by centrifugal acceleration, domain curvature, and Coriolis acceleration can all be independently analyzed. Through numerical modelling, we are thus able to provide insights on the scaling principles and associated inaccuracies of simulating granular flows in a centrifugal acceleration field. These can, in turn, be potentially applied to physical modelling.

The study starts with a review of the centrifugal acceleration field and its relevance to the simulation of kinematic processes. We develop a formulation for dry granular flows in steady state under the influence of an augmented acceleration field in a continuum representation. Based on the insights gained from this representation, we present the implementation and validation of a centrifugal acceleration field in a discrete numerical framework along with its corresponding parametric study. The general features of the DEM simulation of steady-state granular flows under an augmented acceleration field are then discussed, focusing on the effects on the flow characteristic quantities. Finally, these numerical observations are used in the validation of the scaling principles for granular flows down an inclined plane and under a centrifugal acceleration field.

## Granular flows in a centrifugal acceleration field

### Centrifugal acceleration field

A granular flow can be imagined as a collection of rigid particles moving in an organized manner. When triggered inside a geotechnical centrifuge, the particles are immersed in a rotating domain  $(x, y)$  spinning with angular velocity  $\boldsymbol{\omega}$  around an axis  $\mathcal{O}$ . If observed from within the rotational frame, each particle is therefore subject to an apparent acceleration field, which is a function of its distance from the axis  $r$ , its velocity  $\boldsymbol{u}$ , and any other external force as illustrated in Fig. 2.

In a typical experiment in the centrifuge, the rotation axis  $\mathcal{O}$  and the angular rotation vector  $\boldsymbol{\omega}$  are globally defined and kept constant. The centrifugal acceleration  $\boldsymbol{a}_{cf}$ , acts radially outwards from  $\mathcal{O}$ , as:

$$\boldsymbol{a}_{cf} = -\boldsymbol{\omega} \times (\boldsymbol{\omega} \times \boldsymbol{r}). \quad (1)$$

On this rotating domain, each particle is additionally deflected by a virtual Coriolis acceleration  $\boldsymbol{a}_{co}$ :

$$\boldsymbol{a}_{co} = -2\boldsymbol{\omega} \times \boldsymbol{u}. \quad (2)$$

Finally, the external acceleration vector (i.e., gravity  $\boldsymbol{g}$ ) is still active, completing the full centrifugal acceleration field as:

$$\boldsymbol{a} = \boldsymbol{a}_{cf} + \boldsymbol{a}_{co} + \boldsymbol{g} \quad (3)$$

In a laboratory centrifuge, gravity can never be completely ignored. The rotation axis is usually aligned with the vertical, ( $z$  in Fig.1), and therefore gravity acts out of the rotation plane and orthogonal to  $\boldsymbol{a}_{cf}$ . However, with sufficiently large values of  $\boldsymbol{a}_{cf}$ , the effect of gravity is secondary. In a numerical environment, on the other hand, gravity can be completely discounted, a fact that will be exploited later.

A common practice in centrifuge modelling is to relate the magnitude of  $\boldsymbol{a}_{cf}$ , to a representative radius  $R$  in the model, with a scaling factor  $N$  in the form of  $\boldsymbol{a}_{cf} \equiv N\boldsymbol{g} \equiv \omega^2 R$ . With this principle in mind, an experimenter aims to downscale the model dimensions by  $N$  while rotating the model up to a centrifugal acceleration proportional to  $N$ . This scaling keeps the driving acceleration equivalent to that of a system of larger dimensions. The geometric,

kinematic, and dynamic similarities formulated between the scale model and the prototype scenario, are shown in Table 1 (Garnier *et al.*, 2007).

For the case of granular flows in the centrifuge, flow velocity is considered a non-scalable variable (Vallejo *et al.*, 2006; Bowman *et al.*, 2012; Bryant *et al.*, 2015), implying that velocities observed in the scale model are equal to those that would be observed in a prototype  $N$  times larger. However, this reasoning becomes problematic when a prediction of flow velocity is needed prior to the experiment and during the definition of the model-scaling factor. Recent works on granular flows in inclined planes, rotating drums, and flows out of a silo, observed that granular flows under different centrifugal accelerations present a non-linear relation between  $u$  and  $N$  (Dorbolo *et al.*, 2013; Mathews, 2013; Cabrera & Wu, 2017b), that the characteristic length of the flow remains independent of  $N$  (Brucks *et al.*, 2007; Cabrera & Wu, 2017b), and that the flow orientation, relative to the direction of  $\omega$ , plays a dominant role in the mass mobility (Bryant *et al.*, 2015; Cabrera & Wu, 2016).

It is therefore necessary to understand better the effects of the centrifugal acceleration on granular flows, and to consolidate the associated scaling principles. The effects due to the Coriolis acceleration are a particular concern. These are negligible in more traditional geotechnical problems, which typically involve granular material in static conditions, and are therefore still poorly understood. A better understanding of these aspects will allow to fully validate the geotechnical centrifuge as an experimental tool for the study of mass flows.

### Granular flow as a continuum

To partially address the influence of the rotating frame, the granular flow can at a first approximation be represented as a continuum, an approximation reasonable only in the so-called dense (or fluid-like) state. Following the popular and well-documented approach of MiDi (2004), the flow on an infinite inclined plane can be described using a single dimensionless group, the Inertial number  $I$ , which can be interpreted as the ratio between microscopic and macroscopic time-scales (da Cruz *et al.*, 2005):

$$I = \frac{\dot{\gamma} d}{\sqrt{p/\rho}} \quad (4)$$

where  $\dot{\gamma}$  is the shear rate,  $d$  is the particle size,  $p$  is the basal pressure, and  $\rho$  is the particle density. The apparent friction coefficient  $\mu = \tau/p$  of the medium is then assumed to be a simple function of the Inertial number. The resultant constitutive model, relating  $p$  and  $\dot{\gamma}$ , is known as the  $\mu(I)$ -rheology.

Let us consider a dense granular flow of constant volume fraction  $\phi$  and thickness  $h$ , driven by gravity down an infinite flume with constant inclination  $\zeta$  (see Fig. 2). In this case, the  $\mu(I)$ -rheology does not alter the pressure distribution, which remains hydrostatic:

$$p = \rho \phi g \cos \zeta (h - y). \quad (5)$$

Equilibrium also imposes  $\mu = \tan \zeta$ , which determines a constant inertial number  $I$  over the whole depth. The velocity profile can therefore be obtained by plugging the solution for pressure in Equation 4, where  $\dot{\gamma} = \partial u / \partial y$ , and integrating. The result is a Bagnold-like profile, with  $u \propto y^{3/2}$ :

$$u(y^*) = \frac{2}{3} \frac{Ih}{d} u^* y^*, \quad (6)$$

where

$$y^* = 1 - \left(1 - \frac{y}{h}\right)^{3/2}, \quad (7)$$

and  $u^* = \sqrt{gh\phi \cos \zeta}$  is the characteristic velocity, i.e. the local wave speed of the flow (Gray & Edwards, 2014). This is often employed in the definition of the Froude number  $Fr = \langle u \rangle / u^*$ , where  $\langle u \rangle$  is the mean velocity (Gray *et al.*, 2003). For the full derivation, and for an analysis of the influence of the material parameters, please refer to Lagr e *et al.* (2011).

The ultimate goal of centrifuge modeling is to induce an augmented acceleration field  $g \rightarrow Ng$ , with  $N$  the scaling factor. Let us assume that  $\phi$  and  $h$  do not vary significantly when augmenting the acceleration field, as is often observed in laboratory experiments. In this case, only  $p$  and  $u$  are directly influenced by the augmented acceleration. Theoretically, the Inertial number is also unaltered, as it is a simple function of the slope. Note that the validity of this assumption is revisited when discussing the results.

Under these assumptions, pressure scales linearly with  $N$ :

$$p = \rho\phi Ng \cos \zeta (h - y), \quad (8)$$

and the shape of the velocity profile in Equation 6 is not altered, and is therefore still valid. However, the characteristic velocity  $u^*$  is modified, yielding

$$u^* = \sqrt{Ngh\phi \cos \zeta} \quad (9)$$

Under these circumstances and at any point in the flow, velocity scales with  $N^{1/2}$ . In particular, the velocity at the surface ( $y=h$ , or  $y^*=1$ ) is equal to:

$$u(h) = \frac{2}{3} \frac{Ih}{d} u^* \quad (10)$$

This approach gives a first insight into the scaling of velocity in an augmented acceleration field, by showing that velocity  $u(y)$  scales with  $N^{1/2}$ . Note that the same system of equations would have returned a scaling factor  $N$  for velocity if the constitutive model had been Newtonian. The interdependence between pressure and velocity, given by the frictional properties of granular materials, is the origin of the unusual  $N^{1/2}$  scaling.

### Granular flows in a centrifugal acceleration field

The solution becomes more complicated in a rotating reference frame. In addition to the aforementioned assumptions, let us also consider the distance from the rotation axis  $R$  to be constant and much larger than the flow thickness  $h$  (i.e. the centrifugal acceleration field is not curved). In other words, we are considering the inclined plane to be located inside a laboratory centrifuge that is much larger than the flow height. This condition is not easy to obtain in practice, as steady flows are extremely difficult to obtain on an inclined plane inside a laboratory centrifuge. It is however a useful tool, as it allows us to obtain an analytical solution, which can in principle be compared to quasi-steady flows obtained within sufficiently long flumes placed inside a sufficiently large centrifuge.

Neglecting the Coriolis term, acceleration can be rewritten as  $a_{cf} = \omega^2 R$ . The solution is completely analogous to the one obtained in the previous section, provided that  $N = \omega^2 R / g$ . The characteristic velocity  $u^*$  becomes

$$u^* = \sqrt{\omega^2 R h \phi \cos \zeta}. \quad (11)$$

which is analogous to Equation 9.

The full centrifuge acceleration field, including the Coriolis acceleration component, gives a more complex solution. The full field, written in the  $(x, y)$  coordinate system in Fig. 2, is

$$a_x = \omega^2 R \sin \zeta \quad (12)$$

$$a_y = -(\omega^2 R \cos \zeta + 2\omega u), \quad (13)$$

assuming that velocity is always aligned with the  $x$ -axis.

Equation 13 determines a pressure profile in a centrifugal acceleration field of the form:

$$p = \rho \phi (\omega^2 R \cos \zeta + 2\omega u)(h - y), \quad (14)$$

introducing a non-linear dependence between the velocity in the slope direction and the acceleration orthogonal to the plane.

Depending on the sign of  $\omega$ , and on the direction of the flow (the sign of  $u$ ), the product  $\omega u$  in Equation 14 can have positive or negative sign. This has a dramatic importance on the effect of the Coriolis acceleration on the flow structure. A positive product increases the pressure while a negative one reduces it. A reduction in pressure dilates the flow. When pressure falls below hydrostatic values the grain fabric loose coherence, and the dense-flow assumption is no more valid. On the other hand, if the product is positive, the Coriolis acceleration compresses the flow, increasing its stability. Most often, experiments are designed in order to obtain such conditions. Only this case can be safely described using the proposed continuum approach, which is valid for dense flows only. This issue is further discussed in the description of the simulations.

Assuming therefore that the Coriolis acceleration increases pressure, Equation 4 yields the following non-linear governing equation:

$$\frac{\partial u}{\partial y} = \frac{I}{d} \sqrt{\phi (\omega^2 R \cos \zeta + 2\omega u)(h - y)} \quad (15)$$

which, integrated, returns the velocity profile:

$$u(y^*) = \frac{2}{3} \frac{Ih}{d} u^* y^* \left( 1 - \frac{1}{3} I \phi \frac{u_{co}}{u^*} y^* \right), \quad (16)$$

where an additional velocity scale  $u_{co}$  appears, associated with the Coriolis effects:

$$u_{co} = \frac{\omega h^2}{d}. \quad (17)$$

The formulation including  $u_{co}$  is overall slower than the formulation with only  $a_{cf}$  (Equation 10), due to the second term inside the parenthesis in Equation 16. Also, due to the second term, the velocity doesnot monotonically grow with the vertical coordinate  $y$ , but has an inflection at an intermediate height. The overall speed reduction and the position of the flex are governed by the ratio  $u_{co} / u^*$ . Figure 3 illustrates these results graphically. It shows the resultant velocity profiles over a normalized height given by Equation 16 (continuous lines), and compares them with the simpler solution obtained using only  $a_{cf} = \omega^2 R = Ng$  and expressed by Equation 6 (dashed line). The computation parameters are  $d = 0.1$  mm,  $h = 50d$ ,  $N = 50$ ,  $\phi = 0.6$ ,  $\zeta = 24^\circ$ , and  $I = 0.1$  (a common value for steady flows (Andreotti *et al.*, 2013)), which will be further referenced in the analysis of the DEM results.

The Coriolis acceleration alters the flow in a measure that vanishes when  $u_{co} / u^*$  is small, i.e. when  $R/h$  is large. Supercritical flows ( $Fr = \langle u \rangle / u^* > 1$ ) developing within a relatively small centrifuge are slower than the same flows in a larger centrifuge, and get therefore closer to

subcritical conditions (smaller  $Fr$ ). Increasing  $R/h$  produces flows that are closer to the simplified case of flows driven solely by  $Ng$  (or  $a_{cf}$ ).

The velocity profile exhibited in this case has complex origins due to the non-linearity between pressure and velocity. Further, the curvature effects, which have been neglected in the formulation, are bound to substantially alter the velocity profile when  $R$  is small. For this reason, the following sections attempt to answer the validity of the scaling provided by the theoretical formulation, by means of a micro-mechanical model.

### **A numerical model for the centrifuge with DEM**

The simulation strategy is divided in three stages. Firstly, we formulate, implement, and validate a centrifugal acceleration field for a DEM model. Second, we explore the effects of an augmented acceleration field in a granular flow down an inclined plane, as a function of an equivalent scaling factor  $N$ , rotating radius  $R$ , and level of complexity of the acceleration field. Further, we discuss the effects of the augmented acceleration field, explore the parametric space  $(N, R)$  and review the scaling principles for granular flows in a laboratory centrifuge.

#### **Outline of the DEM**

The code used for the simulation is based on the model by Leonardi *et al.* (2016) and is standard in terms of DEM practice. The collision models are described in this study for replicability.

Each grain of the assembly is represented as a spherical particle with mass  $m$  and diameter  $d$ . When particles collide, they do not deform, but a small overlap is allowed in order to compute the repulsive contact forces. Whenever a positive overlap  $\xi$  is registered, contact occurs, and forces are exchanged between the two particles.

In the normal direction, the magnitude of the contact force is set as

$$F_n = k\xi + 2\alpha_n\sqrt{km}\dot{\xi}, \quad (18)$$

where the two parameters  $k$  and  $\alpha_n$  are the stiffness of the contact and the damping coefficient, respectively. This model has the practical advantage of yielding collisions with a constant coefficient of restitution  $c$ :

$$c = \exp\left(-\frac{\pi\alpha_n}{\sqrt{1-\alpha_n^2}}\right). \quad (19)$$

While it is not always true that the collision time is constant, this model is widely employed because of its simplicity, as  $c$  can be easily estimated (Becker *et al.*, 2008).

In the tangential directions, the particles exchange a force of magnitude

$$F_t = \min\left(\mu F_n, 2\alpha_t\sqrt{\frac{2}{7}kmu_t}\right), \quad (20)$$

where  $\alpha_t$  is the tangential damping constant. The tangential force is capped by the Coulomb criterion with a friction coefficient  $\mu$ . The torque is obtained by summing up all the contributions given by the tangential contact forces. The wall-particle contact are modelled in a similar way.

For conventional DEM simulations, the body force is the gravitational force. However, in the local coordinate system of a rotating centrifuge, the centrifugal acceleration field is included as:

$$\mathbf{a} = (\mathbf{F}_n + \mathbf{F}_t) / m + \mathbf{a}_{cf} + \mathbf{a}_{co} + \mathbf{g}, \quad (21)$$

It is noteworthy that  $\mathbf{a}_{cf}$  and  $\mathbf{a}_{co}$  only appear because  $(x, y)$  is the local rotating coordinate system. If the simulation is carried out in the global coordinate system  $(X, Y)$ , e.g. within rotating walls,  $\mathbf{a}_{cf}$ , and  $\mathbf{a}_{co}$  disappear.

### Single particle motion in a centrifugal acceleration field

To validate the implementation of the centrifugal acceleration field in the DEM model, which finds here its first application, two scenarios, illustrated in Fig. 4(a), are tested: first, a single particle with no initial velocity ( $u_0 = 0$ ); and second, a single particle with initial tangential velocity equal and opposite to the velocity of the rotating frame at the same location ( $u_0 = \omega r_0$ ). In the second case, when seen from outside the rotating frame, the particle does not move.

The particles start from the same location in the numerical domain, but are simulated separately. In this case, the simulation domain is a large box with the rotation axis crossing the center, as shown in Fig. 4(a), and bounded by flat frictional walls ( $\mu_w = 0.5$ ).

Figure 4(a) presents the resultant particle trajectories, as seen from inside the rotating frame (i.e. from  $(x, y)$ ). As expected, the particle with no initial velocity moves outwards under the influence of the centrifugal field, until it impacts with the numerical domain boundaries and eventually reaches a corner; while the particle with initial velocity spins around  $\mathcal{O}$ , in a perfect circular trajectory, with no displacements in the radial direction and in agreement with the formulation in Equations 1 and 2. The particle with  $u_0 = 0$  does not move in a straight trajectory, but is deflected by  $a_{co}$  when it gains momentum. Figure 4(b) presents the time evolution of the radial acceleration components  $a_{cf}$  and  $a_{co}$ , normalized by  $\omega^2 r_0$ , with  $r_0$  as the particles initial radial coordinate. At  $t = 0$ , both particles experience the same  $a_{cf} = \omega^2 r_0$ . However, the particle with no initial velocity is affected by  $a_{co} = 0$ ; while the particle with  $u_0 = \omega r_0$  is affected by a Coriolis acceleration  $a_{co} = -2\omega^2 r_0$ , in the direction opposite to  $a_{cf}$ . As the final resulting acceleration is  $a_{co} + a_{cf} = -\omega^2 r_0$ , a circular trajectory is obtained.

The particle that preserves its rotating radius constant around  $\mathcal{O}$  does not experience changes in the acceleration components. In the other scenario, the particle that deflects, perceives a quadratic increase in  $a_{cf}$  and a linear increase in  $a_{co}$  as it moves away from  $\mathcal{O}$ , until it impacts with the boundary. After a series of collisions, the particle reaches its maximum value of  $a_{cf}$  at the corner of the numerical domain, while  $a_{co}$  returns to zero as it deposits there.

### Sample construction

To replicate a realistic granular flow, simulations are performed using a sample of  $N = 7956$  spherical particles of mean particle diameter  $d = 0.1$  mm ( $\pm 10\%$  to limit crystallization), flowing over an inclined plane.

The simulation domain consists of a rectangular box with periodic boundary conditions in the  $x$ - (flow) and  $z$ - (lateral) directions and constrained in the  $y$ - (vertical) direction by walls, as illustrated in Fig. 5. The bottom wall is covered by a layer of randomly distributed particles with an approximate height  $\approx 1.2d$  and with fixed positions throughout the simulation, ensuring a rough base. The rotation axis is located above the particles, and not necessarily inside the simulation box. The vector connecting the rotation axis and the middle of the

bottom wall defines the reference radius of the rotation system  $R$ . Its orientation also defines the tilt of the bottom wall, which for all simulations is fixed at  $\zeta = 24^\circ$ . In this arrangement, the local coordinate system  $(x, y, z)$  remains unaltered and is aligned with the simulation box. When the system rotates, the centrifugal acceleration leads the granular mass to flow down the inclined plane (see Fig. 5). The use of periodic boundary conditions allows for the reproduction of a steady flow. The slope  $\zeta = 24^\circ$  is chosen because particles driven by gravity on an infinite flume with this inclination result in steady uniform dense flows, as proven by Silbert *et al.* (2001), using a similar numerical model and set of parameters. The bottom wall reproduces a tilted flume of infinite length, a common practice in the study of granular flows in steady conditions (Weinhart *et al.*, 2012). The centrifugal acceleration field is not exactly the same at the two periodic walls in direction  $x$ , because their distance to the rotation axis is slightly different. Therefore, particles will experience a small drop in centrifugal acceleration when crossing the boundary. This does not produce any appreciable alteration of the flow at the boundaries. Moreover, when  $R$  is large, the acceleration drop becomes completely negligible, and the system converges towards ideal periodic conditions. The sample is built by randomly distributing the particles inside the simulation domain, and by compacting them by assigning a vertical acceleration  $a_y = -g \cos \zeta$ . When the kinetic energy of the system has vanished, the frame rotation is activated. From this point on, the evolution of the mean surface velocity is monitored, allowing for the identification of the instant at which steady state is reached. This typically occurs within the first 0.3 s.

The resultant column is  $20d$  long,  $10d$  wide, and  $H_0 \approx 35d$  tall, ensuring the simulation of stable flows down an infinite plane, with no local-particle effects (Silbert *et al.*, 2001). The material parameters used in simulations are shown in Table 2. The contact stiffness is chosen in order to reduce computational time, and does not refer to any specific material (Marchelli *et al.*, 2018). However, it is chosen high enough to keep the system within the rigid limit, i.e. in the state where a change in compressibility does not significantly alter the results (Roux & Combe, 2002).

### Simulation space

The numerical experiments are performed under three scenarios. Each has a different level of precision, corresponding to a typical set of simplifications used for interpreting a laboratory centrifuge output.

- A domain where the center of rotation is assumed to be very far from the sample ( $R \gg H_0$ ). In this case, the acceleration field is constant and equal to  $\mathbf{a} = Ng(\sin \zeta, -\cos \zeta, 0)$ . This system is equivalent to a standard flume experiment, but with an augmented gravity field, and could be used as a first simplification for interpreting centrifuge results.
- A rotating domain where the Coriolis acceleration component is deactivated, leaving only the centrifugal acceleration: ( $\mathbf{a} = \mathbf{a}_{cf}$ ). This system allows us to focus on the effects created by the curvature of the acceleration field.
- A rotating domain with a complete acceleration field: ( $\mathbf{a} = \mathbf{a}_{cf} + \mathbf{a}_{co}$ ).

The system kinematics is expected, in every case, to be governed by two dimensionless groups. The first is the scaling factor  $N = \omega^2 R / g$ , with the reference radius  $R$  defined as shown in Fig. 5. The second is the distance from the center of rotation with respect to the

system size  $R/H_0$  (which is equivalent to  $R/h$ ). We explore the results obtained with a parametric matrix where  $N = [1, 2, 5, 10, 20, 50]$  and  $\log(R/H_0) = [3, 4, 5, 6, 7]$ . The two dimensionless groups can be changed independently by altering  $\omega$  and  $R$ . The range of  $R/H_0$  corresponds to  $R/h > 10$  and is in agreement with previous studies and with the assumptions of shallow flows discussed in the continuum formulation. Experimentation below this limit, would present strong effects by the curvature of the acceleration field and be relatively impractical for parametric studies.

In dimensional units, the rotation radius spans from 0.01 m to 3.8 m, since 0.1 mm particles are employed, thus covering the typical size range of laboratory centrifuges. Also very small values of  $R$  are considered, which are impractical but whose simulation is nevertheless important, as it helps to elucidate the minimum dimensions of centrifuge models that renders them free from curvature effects.

As mentioned in the previous section, the Coriolis acceleration can either compress or dilate the flow, depending on the direction of rotation (i.e. the sign of  $\omega$ ). The theoretical framework we present here is only valid for dense flows, which are easily obtainable only if the Coriolis acceleration compresses the flow. In the other case, the flow dilation in the simulations reduces the stability of the flowing mass, leading to difficulties in reaching a dense steady state. Therefore, the sign of  $\omega$  used in the simulation is presented in the next section is chosen in order to obtain Coriolis accelerations that always compress the particles.

## Results and discussion

### Effects on velocity profile

After steady state is obtained, the downslope velocity  $u_x$  and solid fraction  $\phi$  along the flow height are computed. These quantities are obtained by averaging all particle information between layers and over a series of time steps, excluding the transient phase (Weinhart *et al.*, 2013). Using  $\sim 100$  measurements, covering a measurement time of about 0.2 s, all statistics converge.

Time-averaged profiles are presented in Fig. 6 for  $R/H_0 \simeq 10^3$ . Using this radius, the curvature of the centrifugal acceleration field is minimal, and the simulations are close to ideal conditions. The specific effect of curvature will be revisited in the next section. The reference velocity is computed as  $(Ngh\phi \cos \zeta)^{0.5}$ . As expected, when Coriolis acceleration is absent, velocity follows a Bagnold-like profile ( $u(y) \propto y^{\frac{3}{2}}$ ), as predicted by Equation 6.

The profiles with  $a_{cf} + a_{co}$  are slower than in the other two cases. In all simulations,  $\omega$  is aligned with the  $z$ -axis and is positive. Therefore, velocity in  $x$  is generally positive (see Fig. 5), which implies a Coriolis acceleration whose larger component is negative and aligned with  $y$ . Thus, the Coriolis acceleration compresses the flow, and its magnitude grows proportionally to  $u_x$ . As the flow resistance is frictional, this effectively provides a feedback mechanism that checks the flow velocity. In any case, velocity still increases monotonically with  $N$ .

The Coriolis acceleration component also has an effect on the flow profile. When it is active, a variation from the Bagnold scaling is observed, with the profile flattening close to the surface, as predicted by Equation 16. It is important to stress that the Coriolis acceleration term can potentially turn positive by inverting the rotation direction. In this case, it would

have an opposite effect, promoting an expansion and an acceleration of the flow. This case leads to diluted flows, which are not studied in this work.

The solid fraction profiles  $\phi(y)$  do not change shape with  $N$ , presenting slight oscillations across the flow height and sharp drops at the base and free surface, which are a result of the space-averaging algorithm.

### Effects on flow height

Figure 7 presents the variation of flow height  $h$  as a function of  $R/h$  and  $N$ . The  $Ng$  simulations are computed with an uncurved acceleration field (left panels), a hypothesis plausible only if  $R \gg h$ . This is also a common hypothesis used to interpret laboratory results and the reason why efforts are devoted to using large centrifuges and small samples. This scenario, therefore, provide a guide for the eye and refer to an idealized setting. The other two sets of results are obtained with a curved acceleration field. On those two sets, the selected range of  $R$  is intended to present a wide spectrum of model scenarios, with small cases ( $R/h \approx 20$ ), up to large centrifuge radius ( $R/h > 400$ ).

For large enough  $R$  values, the flow height does not show significant variations as a function of  $N$ , due to the low system compressibility. Interestingly, for the scenario with only  $a_{cf}$  (middle panels), an increase in  $N$  results in slightly more dilute flows, probably due to the increased level of agitation of the grains, but this effect is cancelled as an increase in  $R$  densifies the granular flow towards a similar level than in the  $Ng$  case. This is clearly a behaviour caused by curvature effects and suggest a minimum ratio of  $R/h \geq 50$ . Indeed, the two sets with a curved acceleration field have a centrifugal acceleration vector  $\mathbf{a}_{cf}$  with a large deviation from the radial direction, which peaks at  $0.7^\circ$  for  $R/h \approx 20$ . In this range, a dilute layer develops on top of the flowing mass.

In addition to curvature effects, the centrifugal acceleration field  $\mathbf{a}_{cf}$  presents relative variations within the model domain. Specifically, particles at the top of the flume, which are closer to the center of rotation, are accelerated with lower intensity than those at the bottom. Models with small  $R/h$  ratios will suffer the most from this effect, limiting the model capabilities. This requires the definition of a region of interest where a model effective radius has to be defined for setting the scaling principles.

Models with a shorter flume, or models with low tilt have a smaller variation of  $\mathbf{a}_{cf}$  between top and bottom of the flume. In our simulation, the use of periodic boundary conditions allows the creation of a stationary flow on a relatively short flume, thereby partially reducing this problem. These effects become negligible when  $R/h \geq 50$ , with the deviation of  $\mathbf{a}_{cf}$  becoming smaller than  $0.3^\circ$ , and its variation in magnitude within the domain smaller than 0.5%. Moreover, note that the simulations with  $Ng$  are completely free from these effects.

For the scenario including  $a_{cf}$  and  $a_{co}$  (right panels), the resultant flows are thinner ( $\approx 36d$ ), with the curvature disruption effectively checked by the compressive effect of the Coriolis component. For the same reason, in this case, an increase in  $N$  gives rise to slightly denser flows, while an increase in  $R$  leads to slightly thicker flows.

The simulations with  $a_{cf}$  and with  $a_{cf} + a_{co}$  give more similar results when  $R/h$  increases, eventually converging towards the  $Ng$  simplified scenario, and towards a height of  $37d$ . This is a trend common to every measured variable, as will be apparent later. These results suggest that for a system with sufficiently large radius ( $R/h \geq 50$ ) the flow height will present a nearly constant value, consistent with the experimental observations of Brucks *et al.* (2007)

and Cabrera & Wu (2017b). It further confirms that the flow height in a laboratory centrifuge is not controlled by the model acceleration  $N$ , but rather by the particle size and the domain dimensions.

The reference solid fraction  $\phi$  is taken as the average solid fraction computed at the middle section of the flow profiles presented in Fig. 6 (d–e). The variation of  $\phi$  as a function of the rotating radius  $R$  is presented in the inset of Fig. 7, mirroring the variations of  $h$ . The scenario with the augmented acceleration  $Ng$  exhibits a nearly constant value of  $\phi^* = 0.57$ , independent of  $N$ . A clearer view on the curvature effects in the scenario dealing solely with  $a_{cf}$ , suggests that the match with the  $Ng$  scenario occurs for values of  $R/h \geq 50$ , converging to the same value of  $\phi^*$ . In contrast, the scenario with  $a_{cf} + a_{co}$  present, in all cases, slightly denser flows, with density slightly increasing with  $N$ , and close to the maximum for a random close packing of monodisperse spheres  $\phi_{max} \approx 0.64$  (Scott, 1960; Scott & Kilgour, 1969). In any case, a large  $R$  weakens the dependency on  $N$ , and  $\phi$  moves towards  $\phi_{max}$ . Therefore, it is reasonable to conclude that  $\phi$  is constant for the case where  $R/h \geq 50$ , with its scaling independent of  $N$ .

### Effects on flow velocity

After scaling by  $u^*$  (as defined in Equation 9), the velocity profiles do not collapse onto a single trend, as would have been predicted by Equation 6 for the simulations without Coriolis acceleration. Given that the Bagnold scaling is preserved (see Fig. 6), it seems reasonable to suppose that the different simulations are self-similar, and that the incorrect scaling is due to a change in the Inertial number.

The Inertial number is computed by fitting Equation 6 to the velocity profiles obtained in the simulations without the Coriolis acceleration. For the simulations that include the Coriolis acceleration, Equation 16 is used instead. The goodness of fit is always excellent, and the resulting Inertial numbers are shown in Fig. 8. The Inertial number grows as  $I \propto N^{1/6}$ . Note that the obtained values for  $I$  are very sensitive to the domain radius. However, they should eventually converge to those obtained in the  $Ng$  case for large  $R$ . This however has not occurred for the simulation with Coriolis acceleration even at  $\log R/H_0 = 7$ .

It is difficult to be certain about the physics that induces the growth of  $I$ . At  $N = 1$ ,  $I \approx 0.08$ ; therefore the flow state is in the dense regime. It is usually assumed that in this state inertia is negligible, and that the timescale of particle rearrangement is simply proportional to  $p^{1/2}$ . However, an augmented acceleration field might pose an obstacle to particle rearrangement, which would therefore be independent from the confinement pressure, resulting in larger Inertial numbers even in the dense regime.

This is substantiated by the simulations with the Coriolis acceleration. The term  $a_{co}$  has an opposite effect, inducing an increased pressure that is a function of the flow speed, and independent from the flow height. This results in shorter rearrangement times, and lower Inertial numbers.

The unscaled surface velocity (measured at  $y = h$ ,  $y^* = 1$ ) is shown in Fig. 9. The rules for scaling this velocity are suggested by rearranging Equation 10:

$$\frac{u(h)}{u^*} = \frac{2}{3} \frac{Ih}{d}, \quad (22)$$

where  $u^* \propto N^{1/2}$ . However, the characteristic velocity  $u^*$  is a good scaling quantity only if the inertial number  $I$  is constant, while it is clear from Fig. 8 that this is not the case. The scaling law should therefore be reformulated taking into account the variation of the Inertial

number. A simple solution is to scale also by the Inertial number ( $I \propto N^{1/6}$ ), which can be empirically obtained using the results illustrated in Fig. 8. This scaling is validated in the inset of Fig. 9. The inset presents the result of the normalization of  $u(h)$  by  $Iu^*$ . In this way, the scaling factor for surface velocity becomes  $Iu^* \propto N^{1/6} \cdot N^{1/2} = N^{2/3}$  which yields excellent results, especially for large  $R$ .

Like any other macroscopic feature of the flow, velocity presents a dependence on the rotation radius  $R$ , again given by the disruptive effect of the curvature. There is a clear difference between the scenarios that include, or not, the Coriolis acceleration component  $a_{co}$ . When included,  $u$  increases as a function of  $R$ ; without it,  $u$  decreases as a function of  $R$ , approaching on both cases to the scenario driven by  $Ng$ .

Figure 10 presents the effect of  $R$  on the surface velocity, normalized by the characteristic velocity  $u^* = (Ngh \cos \zeta)^{1/2}$ . As already observed for the flow height, the scenario with only the centrifugal acceleration component converges to the simplified case of  $Ng$  at  $R/h \geq 50$ , reinforcing the argument of the marginal effects of the curvature of the acceleration field when  $R$  is large.

For the scenario with  $a_{cf} + a_{co}$ , it is shown that by increasing  $R$ , the model velocity increases. This was predicted by Equation 16, where the second term inside the brackets, which is constant with respect to  $R$ , becomes negligible with respect to the first term and predicts  $u \propto \sqrt{R}$ . In fact, subtracting Equation 10 from Equation 16, one can estimate the influence of the Coriolis acceleration component on the surface velocity  $u_{co}$  as:

$$\Delta u_{co} = -\frac{2}{9} \frac{\omega I^2 \phi h}{d} u_{co}, \quad (23)$$

thus predicting a reduction in velocity due to the Coriolis acceleration component, which is

$$\frac{u_{co}}{u^*} \propto I^2 \frac{u_{co}}{u^*}. \quad (24)$$

If the Inertial number is conserved,  $u_{co}/u^*$  should decay as  $1/R^{0.5}$ . The numerical results qualitatively reproduce this observation, but with a slightly lower exponent ( $1/R^{0.3}$ ). This is due to changes in the Inertial number, which grows with  $R$ . Unfortunately, with the current data sets, it is not possible to confirm whether by further increasing  $R/h$ , all scenarios will collapse towards the equivalent trend of  $Ng$ , but it appears reasonable, given that the Inertial number also converges to the values recorded with  $Ng$  for growing  $R$  (see Fig. 8).

Although Equation 16 qualitatively describes the behavior observed in Fig. 10, there is no quantitative agreement between theory and simulations. This might be due to the change in the Inertial number induced by the Coriolis acceleration, which is not accounted for in the theory leading to Equation 16. This considerably extends the range of  $R/h$  where the Coriolis acceleration influences the flow structure.

### Effects on basal forces

Overall, one of the main motivations of employing the centrifugal acceleration field is the stress scaling within the material, which becomes equivalent to that of a prototype of larger dimensions (Wood, 2003). The force measured at the base  $f_b$ , normalized by the overall mass  $m$  and the equivalent acceleration factor  $Ng$  is shown in Fig. 11. As expected, the simplified scenario of  $Ng$  falls around unity, acting as an indicator of the force equilibrium between driving and resultant forces in the  $y$  direction.

Similar to the previous cases, the scenario driven solely by  $a_{cf}$  converges towards the  $Ng$  scenario, giving values below unity at a small rotating radius that can be regarded as the result of curvature effects. For the scenario  $a_{cf} + a_{co}$ , the total weight is apparently increased by the Coriolis accelerations. This effect is once more controlled by  $u_{co}/u^*$ , and becomes negligible when the rotating radius becomes large. While a marginal error is present even for large values of  $R/h$ , it is acceptable to consider that  $f_b$  scales linearly with  $N$ .

Finally, the stress distribution for steady uniform flows allows the definition of an effective friction  $\mu$ , defined as the ratio between tangential and normal forces at the base  $f_{yx}/f_{yy}$ , which should be equal to  $\tan \zeta$  on an inclined plane. Figure 12 presents how the different simulation scenarios converge towards this value, presenting a greater convergence for larger values of  $N$  and  $R$  and differentiating between the rotating scenarios with and without  $a_{co}$ . For the scenario with  $a_{cf} + a_{co}$ , the apparent increase in the flow weight given by the Coriolis acceleration determines an apparent lower basal friction, eventually converging towards  $\tan \zeta$  for large  $R/h$ .

### Conclusions and outlook

In this work, we employ a numerical setup to reproduce a steady granular flow inside a rotating reference frame. The frictional nature of the material predicts a peculiar scaling, with velocity  $u$  scaling with  $N^{1/2}$ . However, the augmented acceleration has multiple secondary effects. We notice an apparent increase in the Inertial number of the flow, empirically observed to be proportional to  $N^{1/6}$ . This variation might be due to inertial effects becoming relevant when the acceleration is augmented. As a consequence, the scaling factor for velocity changes to  $N^{1/6} * N^{1/2} = N^{2/3}$ . This scaling has proven to be very resilient to changes in the system, if  $R$  is sufficiently large. Moreover, the explored simulation space confirms that under an augmented acceleration field the flow thickness and solid volume fraction are independent of  $N$ .

Intuitively, a large radius is beneficial because it reduces the spurious effects created by the curvature of the centrifugal acceleration field and by the Coriolis acceleration components. We observed that when  $R/h > 50$ , the curvature effects can be safely neglected. Below this value, results from physical modelling are bound to be severely altered by both curvature effects and the Coriolis acceleration. The design of mass flow experiments should therefore always keep  $R/h > 50$  as a minimum for avoiding at least the curvature effects.

A simple frictional model predicts that Coriolis acceleration reduces the velocity of the flow proportionally to  $Iu_{co}/u^*$ . This dimensionless group becomes very small already at  $R/h=100$ , but the velocity reduction is significant in the numerical experiments even at much larger values ( $R/h > 1000$ ). One can speculate that this is due to the non-constant Inertial number, which probably invalidates the scaling, giving a much slower convergence. In fact, if the Coriolis acceleration is included,  $I \propto N^{1/6}$  still holds, but an overall reduction of the Inertial number is observed. This reduction further diminishes with  $R$ , but was found to be always significant in the performed tests. This is probably due to the flow compression induced by the Coriolis acceleration.

In any case, the set of  $R$ -values studied in the current research spans the typical length scales of laboratory centrifuge experiments. Effects due to the Coriolis accelerations, albeit difficult to quantify, should therefore always be expected. It would be interesting to simulate a system where the confining pressure and gravity can be changed independently. This would help to

clarify when a change of state can occur in the centrifuge due to an apparent increase in inertia.

Additionally, the effect of the sign of  $\omega$  remains to be explored by the authors. In our simulations, the Coriolis acceleration always compresses the particles, therefore opposing the flow. However, a rotation in the opposite direction would determine an identical centrifugal acceleration, but a Coriolis acceleration of opposite direction, therefore dilating (and destabilizing) the flow. Similar problems are experienced when the flume is steeper. Experimental observations by Bryant *et al.* (2015) have proven that steeper slopes lead to higher flow velocities for the same driving acceleration (i.e.,  $Ng$ ), magnifying the effects of the Coriolis acceleration. These cases were not addressed in this paper, and clearly more studies are needed to understand them better. A possible solution would be to implement a theory that is suitable for the description of the dilute state (e.g. kinetic theory for granular flows as in (Jenkins & Berzi, 2012)).

### Acknowledgements

M.A.C. received funding from the Universidad de los Andes, Early-stage Researcher Fund (FAPA) under Grant No. PR.3.2016.3667. A.L. would like to thank Prof. Pirulli for ongoing financial support. Computational resources were provided by HPC@POLITO, a project of Academic Computing within the Department of Control and Computer Engineering at Politecnico di Torino (<http://www.hpc.polito.it>). The authors would like to thank Ricardo Morales, from the Universidad de los Andes, for his assistance with data fitting.

### Notation

$a_{cf}$	centrifugal acceleration ( $m/s^2$ )
$a_{co}$	Coriolis acceleration ( $m/s^2$ )
$c$	restitution coefficient (-)
$d$	particle diameter (m)
$F_n$	normal contact force ( $kg\ m/s^2$ )
$F_t$	tangential contact force ( $kg\ m/s^2$ )
$g$	gravity ( $m/s^2$ )
$h$	flow height (m)
$H_0$	initial flow height (m)
$I$	Inertial number (-)
$k$	normal contact stiffness (N/m)
$m$	particle mass (kg)
$N$	scaling factor (-)
$p$	flow pressure ( $kg\ m/s^2$ )
$R$	centrifuge radius (m)
$u$	flow velocity (m/s)
$u^*$	flow characteristic velocity (m/s)
$u_{co}$	Coriolis reference velocity (m/s)
$\alpha_n$	normal damping coefficient (-)
$\alpha_t$	tangential damping coefficient (-)
$\dot{\gamma}$	flow shear rate (1/s)
$\mu$	friction coefficient (-)

$\phi$	solid volume fraction (-)
$\omega$	angular velocity (1/s)
$\rho$	particle mass density (kg/m <sup>3</sup> )
$\xi$	particle overlap (m)
$\zeta$	incline slope (°)

## References

- Andreotti, B., Forterre, Y. & Pouliquen, O. (2013). *Granular media. Between fluid and solid*. Cambridge Univ. Press.
- Becker, V., Schwager, T. & Pöschel, T. (2008). Coefficient of tangential restitution for the linear dashpot model. *Physical Review E - Statistical, Nonlinear, and Soft Matter Physics* **77**, 1–12, doi:10.1103/PhysRevE.77.011304, 0708.3401.
- Bowman, E., Take, A., Rait, K. & Hann, C. (2012). Physical models of rock avalanche spreading behaviour with dynamic fragmentation. *Canadian Geotechnical Journal* **49**, No. 4, 460–476, doi: 10.1139/t2012-007, URL <http://dx.doi.org/10.1139/t2012-007>, <http://dx.doi.org/10.1139/t2012-007>.
- Brucks, A., Arndt, T., Ottino, J. M. & Lueptow, R. M. (2007). Behavior of flowing granular materials under variable  $g$ . *Phys. Rev. E* **75**, 032301, doi: 10.1103/PhysRevE.75.032301, URL <http://link.aps.org/doi/10.1103/PhysRevE.75.032301>.
- Bryant, S., Take, W., Bowman, E. & Millen, M. (2015). Physical and numerical modelling of dry granular flows under coriolis conditions. *Géotechnique* **65**, No. 3, 188–200, doi: 10.1680/geot.13.P.208, <http://www.icevirtuallibrary.com/doi/pdf/10.1680/geot.13.P.208>.

Accepted manuscript doi:  
10.1680/jgeot.18.p.260

---

Cabrera, M. & Wu, W. (2016). Space–time digital image analysis for granular flows.

*International Journal of Physical Modelling in Geotechnics* doi:

10.1680/jphmg.16.00018.

Cabrera, M. & Wu, W. (2017a). Scale model for mass flows down an inclined plane in a geotechnical centrifuge. *Geotechnical Testing Journal* **40**, No. 4, 719–730, doi:

10.1520/GTJ20160044, <http://dx.doi.org/10.1680/jphmg.16.00018>.

Cabrera, M. A. & Wu, W. (2017b). Experimental modelling of free-surface dry granular flows under a centrifugal acceleration field. *Granular Matter* **19**, No. 4, 78, doi:

10.1007/s10035-017-0764-z, URL <https://doi.org/10.1007/s10035-017-0764-z>.

da Cruz, F., Emam, S., Prochnow, M., Roux, J.-N. & Chevoir, F. (2005). Rheophysics of dense granular materials: Discrete simulation of plane shear flows. *Physical Review E* **72**, No. 2, 021309, doi: 10.1103/PhysRevE.72.021309.

Dorbolo, S., Maquet, L., Brandenbourger, M., Ludewig, F., Lumay, G., Caps, H.,

Vandewalle, N., Rondia, S., Mélard, M., van Loon, J., Dowson, A. & Vincent-

Bonnieu, S. (2013). Influence of the gravity on the discharge of a silo. *Granular Matter* **15**, 263–273, doi: 10.1007/s10035-013-0403-2.

Froude, M. J. & Petley, D. N. (2018). Global fatal landslide occurrence from 2004 to 2016.

*Natural Hazards and Earth System Sciences* **18**, No. 8, 2161–2181, doi:

10.5194/nhess-18-2161-2018.

Garnier, J., Gaudin, C., Springman, S., Culligan, P., Goodings, D., König, D., Kutter, B.,

Phillips, R., Randolph, M. & Thorel, L. (2007). Catalogue of scaling laws and

similitude questions in geotechnical centrifuge modelling. *International Journal of Physical Modelling in Geotechnics* **7**, No. 3, 1–23.

Gray, J. & Edwards, A. (2014). A depth-averaged  $\mu(i)$ -rheology for shallow granular free-surface flows. *Journal of Fluid Mechanics* **755**, 503–534.

Gray, J. M. N. T., Tai, Y.-C. & Noelle, S. (2003). Shock waves, dead zones and particle-free regions in rapid granular free-surface flows. *Journal of Fluid Mechanics* **491**, 161–181, doi: 10.1017/S0022112003005317.

Gue, C. S. (2012). *Submarine landslide flows simulation through centrifuge modelling*. Ph.D. thesis, University of Cambridge.

Hungr, O. & Jakob, M. (2005). *Debris-flow Hazards and Related Phenomena*. Springer-Verlag Berlin Heidelberg, doi: 10.1007/b138657.

Iverson, R. (2015). Scaling and design of landslide and debris-flow experiments. *Geomorphology*.

Jenkins, J. T. & Berzi, D. (2012). Kinetic theory applied to inclined flows. *Granular Matter* **14**, No. 2, 79–84, doi: 10.1007/s10035-011-0308-x, URL <https://doi.org/10.1007/s10035-011-0308-x>.

Lagrée, P.-Y., Staron, L. & Popinet, S. (2011). The granular column collapse as a continuum: validity of a two-dimensional navier–stokes model with a  $\mu(i)$ -rheology. *Journal of Fluid Mechanics* **686**, 378–408, doi: 10.1017/jfm.2011.335.

Leonardi, A., Cabrera, M., Wittel, F. K., Kaitna, R., Mendoza, M., Wu, W. & Herrmann, H. J. (2015). Granular-front formation in free-surface flow of concentrated suspensions.

- Leonardi, A., Pokrajac, D., Roman, F. & Zanello, F. (2018). Surface and subsurface contributions to the build-up of forces on bed particles. *Journal of Fluid Mechanics* **851**, 558–572, doi: 10.1017/jfm.2018.522.
- Leonardi, A., Wittel, F. K., Mendoza, M., Vetter, R. & Herrmann, H. J. (2016). Particle-Fluid-Structure Interaction for Debris Flow Impact on Flexible Barriers. *Computer-Aided Civil and Infrastructure Engineering* **31**, No. 5, 323–333, doi: 10.1111/mice.12165, 1409.8034.
- Marchelli, M., Leonardi, A. & Pirulli, M. (2018). On the efficiency of slit dams in retaining granular flows. *Under review for Géotechnique* .
- Marin-Ferrer, M., Vernaccini, L., & Poljansek, K. (2017). Index for risk management inform concept and methodology report - version 2017. doi: 10.2760/094023.
- Mathews, J. (2013). *Investigation of granular flow using silo centrifuge models*. Ph.D. thesis, University of Natural Resources and Life Sciences, Vienna.
- MiDi, G. (2004). On dense granular flows. *The European Physical Journal E* **14**, No. 4, 341–365, doi: 10.1140/epje/i2003-10153-0, URL <http://dx.doi.org/10.1140/epje/i2003-10153-0>.
- Nadim, F., Kjekstad, O., Peduzzi, P., Herold, C. & Jaedicke, C. (2006). Global landslide and avalanche hotspots. *Landslides* **3**, No. 2, 159–173.

- Ng, C. W. W., Choi, C. E., Koo, R., Goodwin, G. R., Song, D. & Kwan, J. S. (2017). Dry granular flow interaction with dual-barrier systems. *Géotechnique* **68**, No. 5, 386–399.
- Roux, J. N. & Combe, G. (2002). Quasistatic rheology and the origins of strain. *Comptes Rendus Physique* **3**, No. 2, 131–140, doi: 10.1016/S1631-0705(02)01306-3, 0901.2846.
- Scott, G. (1960). Packing of spheres: Packing of equal spheres. *Nature* **188**, No. 4754, 908–909, URL <http://dx.doi.org/10.1038/188908a0>.
- Scott, G. & Kilgour, D. (1969). The density of random close packing of spheres. *Journal of Physics D: Applied Physics* **2**, No. 6, 863, URL <http://stacks.iop.org/0022-3727/2/i=6/a=311>.
- Silbert, L. E., Ertas, D., Grest, G. S., Halsey, T. C., Levine, D. & Plimpton, S. J. (2001). Granular flow down an inclined plane: Bagnold scaling and rheology. *Phys. Rev. E* **64**, 051302, doi: 10.1103/PhysRevE.64.051302, URL <https://link.aps.org/doi/10.1103/PhysRevE.64.051302>.
- Song, D., Ng, C. W. W., Choi, C., Zhou, G. G., Kwan, J. S. & Koo, R. (2017). Influence of debris flow solid fraction on rigid barrier impact. *Canadian geotechnical journal* **54**, No. 10, 1421–1434.
- Vallejo, L., Estrada, N., Taboada, A., Caicedo, B. & Silva, J. (2006). Numerical and physical modeling of granular flow. In *Physical Modelling in Geotechnics* (Ng, C., Wang, Y. & Zhang, L., eds.), Taylor & Francis, pp. –, doi: 10.1201/NOE0415415866.ch207, URL <http://dx.doi.org/10.1201/NOE0415415866.ch207>.

Weinhart, T., Hartkamp, R., Thornton, A. R. & Luding, S. (2013). Coarse-grained local and

objective continuum description of three-dimensional granular flows down an

inclined surface. *Physics of Fluids* **25**, No. 7, 070605, doi: 10.1063/1.4812809.

Weinhart, T., Thornton, A. R., Luding, S. & Bokhove, O. (2012). Closure relations for

shallow granular flows from particle simulations. *Granular Matter* **14**, No. 4, 531–

552, doi: 10.1007/s10035-012-0355-y, 1108.5033.

Wood, D. (2003). *Geotechnical modelling*, vol. 1. CRC Press.

Table 1. Relevant scaling principles for mass flows in a centrifuge, between a model and a

prototype (Garnier *et al.*, 2007). The scale factor is  $N \equiv \omega^2 R$ .

Quantity	Prototype (field)	Model (centrifuge)
Pressure	$\sigma$	$\sigma$
Strain	$\varepsilon$	$\varepsilon$
Density	$\rho$	$\rho$
Length	$L$	$L / N$
Time	$t$	$t / N$
Force	$F$	$F / N^2$
Velocity	$u$	$U$
Acceleration	$\dot{u}$	$N\dot{u}$

Table 2. Material parameters used in the numerical simulations.

Parameter	Value
Mass density $\rho$	2000 kg / m <sup>3</sup>
Mean particle diameter $d$	10 <sup>-4</sup> m
Contact stiffness $k$	100 N / m
Restitution coefficient $c$	0.88
Tangential damping constant $\alpha_t$	0.5
Friction coefficient $\mu$	0.5

**Figure captions**

Figure 1. Example of a centrifuge model for the study of granular flows (adapted from Cabrera & Wu (2016))

Figure 2. Centrifugal acceleration field components  $a_{cf}$  and  $a_{co}$  on a single particle with local velocity  $u_i$ . The global coordinate system  $(X;Y)$  with particle  $i$  rotating around  $\mathcal{O}$  at a distance  $r_i$  and at an angular velocity  $\omega$ .

Figure 3. Normalized velocity profile  $u$  for a scaled acceleration at  $N = 50$ . All plots are done with material parameters:  $d = 0.1$  mm,  $h = 50d$ ,  $\phi = 0.6$ ,  $\zeta = 24^\circ$ , and  $I = 0.1$ .

Figure 4. Simulation of two single particles rotating around  $\mathcal{O}$ , starting in  $+$  and ending in  $\bullet$ . (a) Trajectories of the particle seen from the rotating reference  $(x, y)$ , with no initial motion in the numerical domain ( $u_0 = 0$ ) and with initial tangential velocity equal and opposite to  $\omega$  ( $u_0 = \omega r_0$ ). (b) Evolution of the acceleration components magnitude,  $a_{cf}$  and  $a_{co}$  for the corresponding particles.

Figure 5. Snapshot of the 3D simulation domain for  $N = 7956$  over a roughened bottom (in dark grey)  $1.2d$  thick of randomly distributed fixed particles, and tilted at  $\zeta = 24^\circ$ . The flow is directed down the incline. The transparent boxes on the  $y$ - $z$  and  $x$ - $y$  planes are periodic boundaries on the  $x$ - (flow) and  $z$ - (lateral) directions.

Figure 6. (top row) normalized velocity profiles  $u/u^*$  as a function of  $N$ , (bottom row) solid fraction profiles  $\phi$  as a function of  $N$  at  $R/H_0 = \exp(7)$ . When  $a_{co}$  is active (right panels) the flow becomes slower and the solid fraction increases. Note that the velocity profiles are replicated by the analytical model in Equation 6 and Equation 16, respectively, by fitting the inertial number  $I$  to the simulation output (dashed lines on top row).

Figure 7. Variation of normalized flow height  $h/d$  for the three acceleration scenarios, as a function of the normalized rotating radius  $R$  and flow height  $h$ , keeping  $N$  constant.

Figure 8. Inertial numbers computed by fitting the velocity profiles obtained by Equation 6 and Equation 16 to the simulations results with and without Coriolis acceleration for the largest value of  $R$ , respectively.

Figure 9. Variation of surface velocity as a function of the scaling factor  $N$ , for the different rotating radius  $R$ . In inset: Normalization of the surface velocity by the characteristic velocity  $u^* = (Ngh \cos \zeta)^{1/2}$  and the Inertial number  $I$ .

Figure 10. Variation of surface velocity, normalized by the characteristic velocity  $u^* = (Ngh \cos \zeta)^{0.5}$  and Inertial number  $I$ , as a function of normalized rotating radius  $R/h$ . Note that the discrepancy between the analytical model in Equation 16 and simulations with  $a_{co}$  results from the dependency of  $I$  with  $N$ .

Figure 11. Evolution of the basal force  $f_b$  normalized by the flow mass  $m$  and equivalent acceleration  $Ng$  as a function of the normalized rotating radius  $R/h$ . Note that  $f_b / mNg = 1$  implies that the system is in mechanical equilibrium.

Figure 12. Variation of the effective friction  $\mu_{eff}$  as a function of normalized rotating radius  $R/h$ . Note that  $\mu_{eff}$  approaches the value of  $\tan \zeta$ .

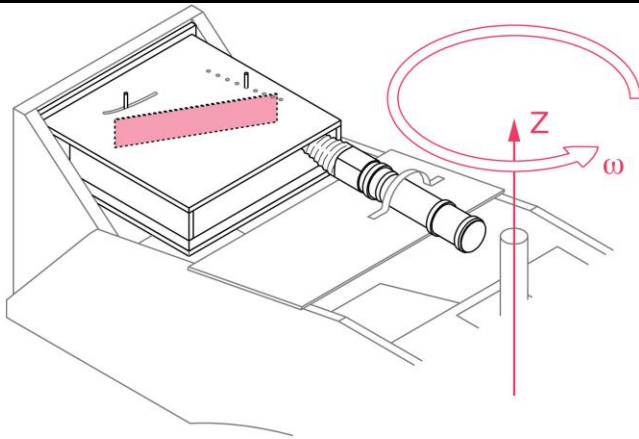


Fig. 1.

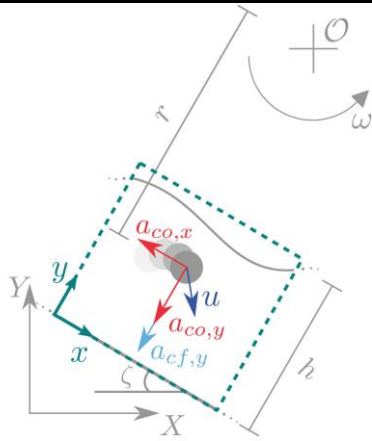


Fig. 2.

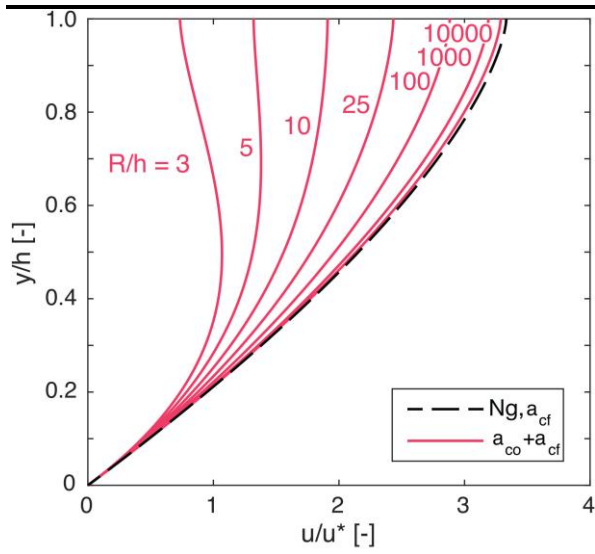


Fig. 3.

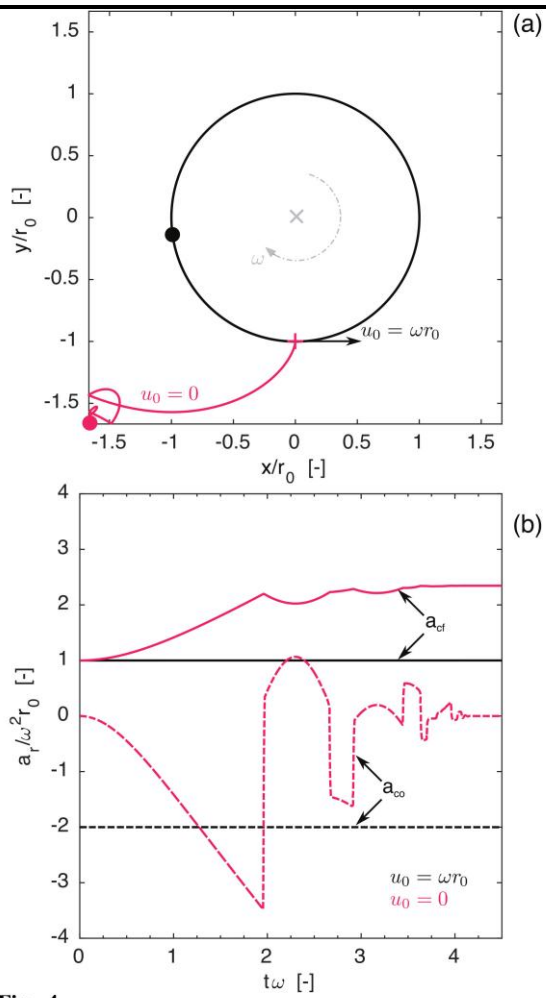


Fig. 4.

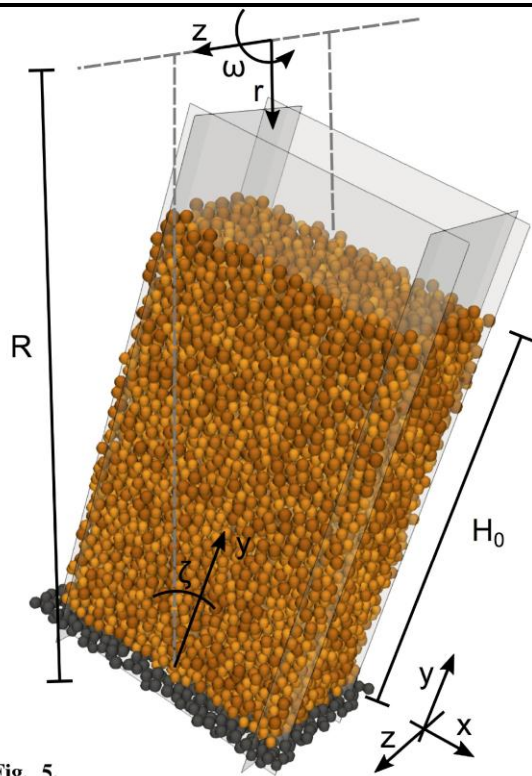


Fig. 5.

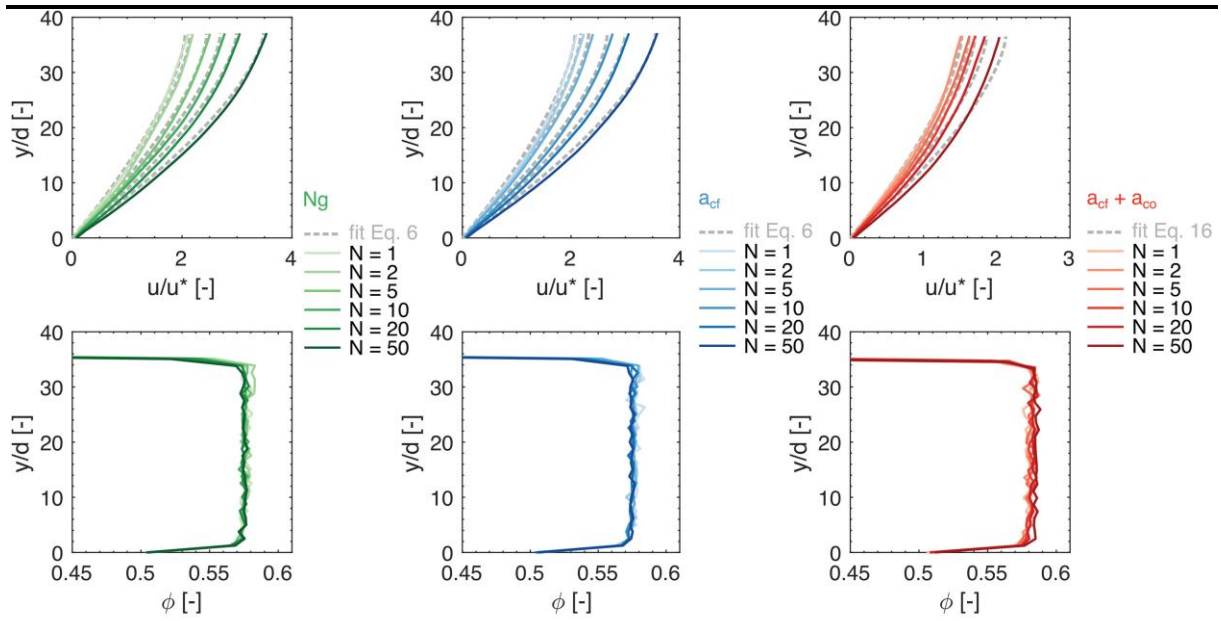


Fig. 6.

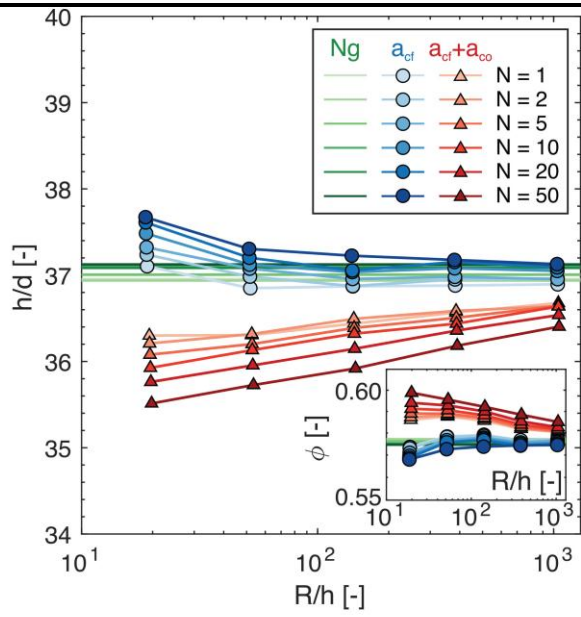


Fig. 7.

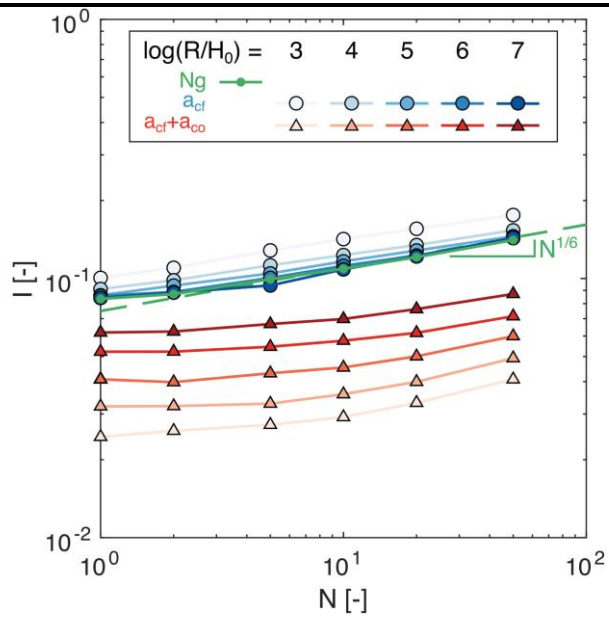


Fig. 8.

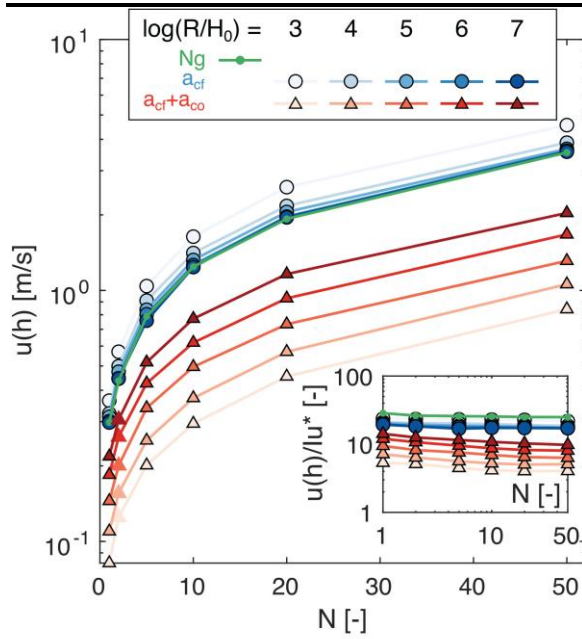


Fig. 9.

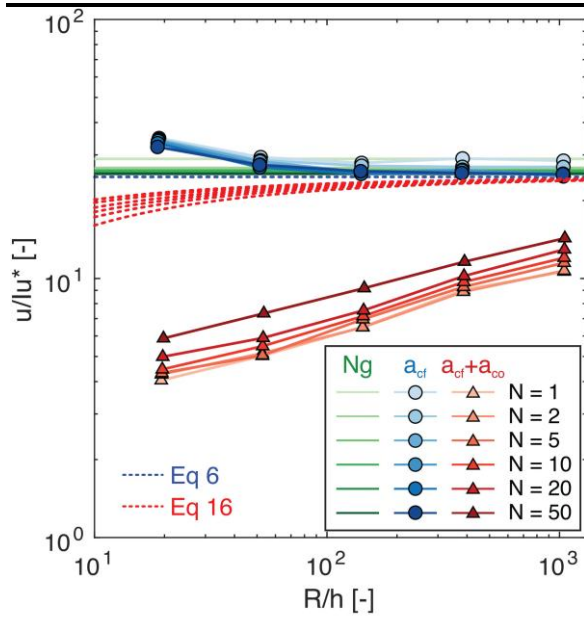


Fig. 10.

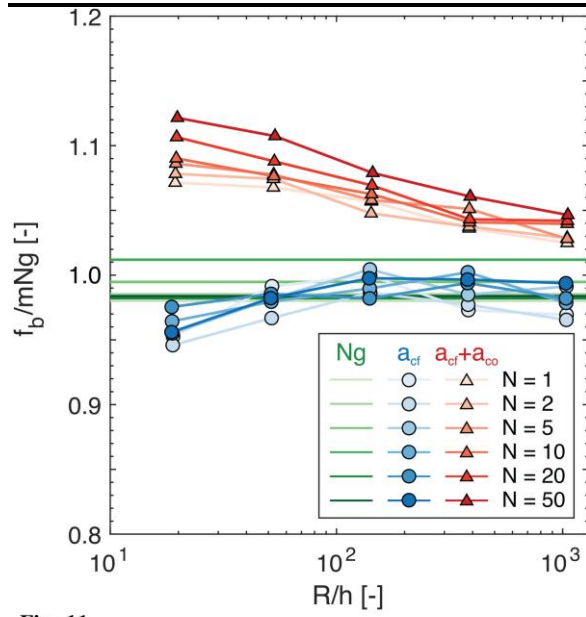


Fig. 11.

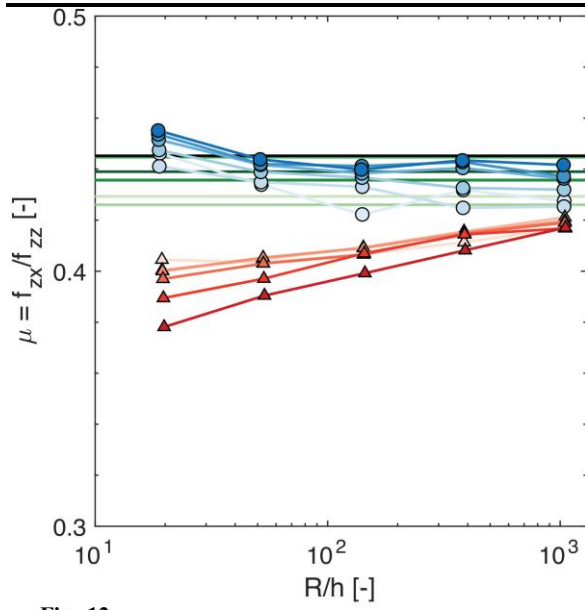


Fig. 12.